The synthesis of CoAl$_{0.3}$Fe$_{1.7}$O$_4$/SmFeO$_3$ nanocomposites with enhanced properties for technological applications

Ebtesam E. Ateia[1,a)], K. K. Meleka[1], Charanjeet Singh[2], F. Z. Ghobrial[1], A. El-Bassuony[1], Dalia N. Ghafar[1]

[1] Faculty of Science, Physics Department, Cairo University, Giza 12613, Egypt
[2] School of Electronics and Electrical Engineering, Lovely Professional University Phagwara, Punjab, India
a) Address all correspondence to this author. e-mail: drebtesam2000@yahoo.com; ebtesam@sci.cu.edu.eg

The main challenge of the current study is to produce nanocomposites (NCs) of (1-x) CoAl$_{0.3}$Fe$_{1.7}$O$_4$ /(x) SmFeO$_3$ with improved structural and magnetic properties using the citrate auto-combustion technique. High-resolution transmission electron microscopy images showed nanostructures with average particle sizes of 32.5 and 52.5 nm for SmFO$_3$ and CoAl$_{0.3}$Fe$_{1.7}$O$_4$, respectively. The anisotropy constant values for $x = 0.3$ are nearly 11 times greater than SmFeO$_3$. The ratio of SmFeO$_3$ incorporated into NCs adjusts their switching field distribution (SFD), making NCs with a low SFD recommended for recording applications. NCs offer the combined advantages of the two constituent phases and can be used to create new and more advanced applications. Based on the estimated data, the prepared NCs can operate at a frequency between 0.1 and 11.9 GHz, making them suitable for developing nanotechnology devices from radio waves traveling through the S-band to the Ku band.

Introduction

The study of multiple phases and crystal structures is a highly advantageous scientific field for obtaining a wide range of advanced physical and magnetic properties. The resulting materials, with their modified and advanced characteristics, hold great promise for various industrial applications. Nanocrystals (NCs) are used to create novel materials with superior quality, modification, and diverse properties [1–5]. Among these materials the spinel structure which is cubic, is known for its excellent magnetic properties and stability. On the other hand, the perovskite structure is recognized for its high structural flexibility, allowing it to accommodate a wide range of cations and leading to diverse physical properties such as ferro electricity. The presence of spinel-perovskite phases in a prepared composite structure can significantly impact the material's properties and performance. The specific effect will depend on the intended application, the chosen materials for the spinel and perovskite phases, and the interaction between these phases. Including spinel structures can enhance the overall stability and magnetic properties of the perovskite phase, particularly at high temperatures or during thermal

cycling, which is advantageous for applications like solid oxide fuel cells (SOFCs).

One of the most significant classes of materials is rare earth perovskites (REFeO$_3$), which have attracted considerable interest due to their unique physical and magnetic properties [6–9]. Samarium perovskite (SFO) is particularly noteworthy for its exceptional magnetic behavior and a band gap comparable to that of a semiconductor (2–3 eV), making it a subject of research in the gas sensing field [10]. Its suitability for room temperature device applications is evident from its high spin switching and reorientation temperatures of 278.5 K and 480 K, respectively [11]. Furthermore, SFO exhibits remarkably rapid magnetic switching and easy axis rotation [12]. Due to the Dzyaloshinsky-Moriya anisotropic exchange interaction and high dielectric constant, SFO displays weak ferromagnetic behavior and inappropriate ferro electricity [13].

Nano-sized cobalt spinel ferrite (CoFe$_2$O$_4$) has unique properties in technology, including its intriguing structural, magnetic, electrical, and optical properties [14–16]. The introduction of aluminum (Al) cations can alter the crystal size, effective bond lengths, lattice constant, crystalline

density, and cation distribution between A and B-sites, consequently modifying its physical properties [17–20]. Additionally, the addition of Al reduces the magnetization of the material and adjusts its hard and soft hysteresis loops, making $CoFe_{2-x}Al_xO_4$ suitable for high-frequency applications [21].

The objective of this study is to prepare CAFO-SFO NCs with customizable magnetic properties suitable for use in magnetic recording media, sensors, and biomedical devices. The NCs also cover a range of frequencies suitable for nanotechnology devices operating at higher frequencies. The preparation process allows for the adjustment of particle size, shape, and composition to meet specific application requirements and enhance performance and functionality.

The study aims to synthesize NCs made of multiferroic perovskite (SFO) and magnetic spinel (CAFO) using the citrate auto-combustion method. The goal is to improve the structural and magnetic properties of the prepared NCs to expand their potential applications.

Results and discussion

Structural analyses

XRD analysis

Figure 1 shows the XRD diagram testing for the presence of two phases, cubic and orthorhombic, in the NCs. The absence of impurities confirms that there is no chemical reaction. The ICDD card codes (01-083-4767) and (04-009-8408) are used as references to identify and index the peaks corresponding to the cubic structure with the main peak at $2\theta = 35.608^o$ with indices (311) and the orthorhombic structure at $2\theta = 32.649^o$ with indices (112). The intensity of SFO peaks decreases as the content of CAFO increases in the NCs. This decrease in intensity is attributed to small structure defects and stress changes caused by the substitution of cations. These substitutions result in minimal changes in peak positions [22]. The tolerance factor (T) can be used to determine the symmetry and stability of the resultant structure, which depend on the relative sizes of the
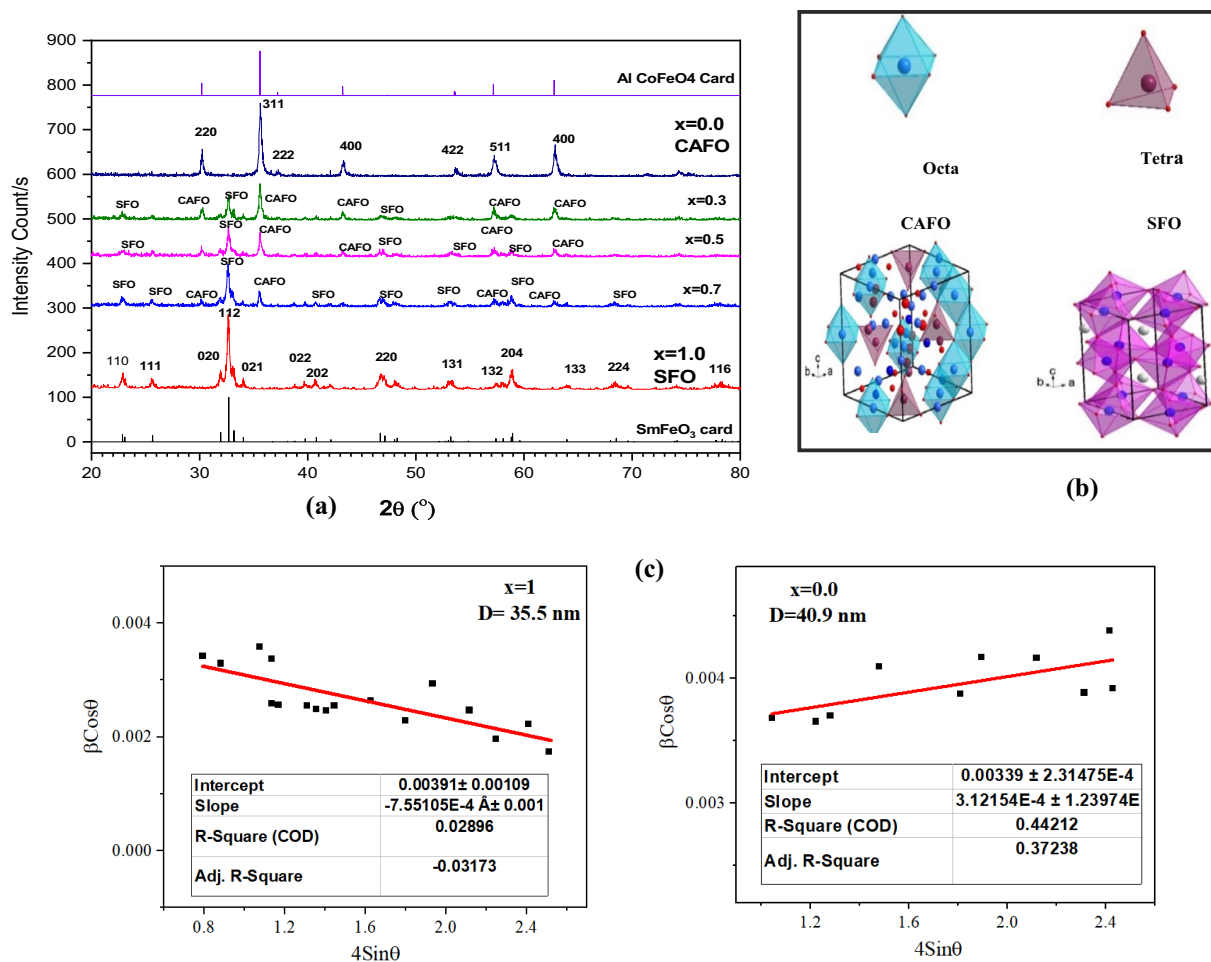

Figure 1: (a) XRD diagram for (1-x) CAFO + (x) SFO NCs (0.0 ≤ x ≤ 1), (b) crystal structure pattern of CAFO and SFO phases, (c) Williamson-Hall plots.

cations [23]. The Goldschmidt relation provides the T value for the perovskite phase [24].

$$T = \frac{r_A + r_O}{\sqrt{2}(r_B + r_O)} \tag{1}$$

On the other side, (T) for spinel phase is given by [25, 26]:

$$T = \frac{1}{\sqrt{3}}\left(\frac{r_A + r_O}{r_B + r_O}\right) + \frac{1}{\sqrt{2}}\left(\frac{r_O}{r_B + r_O}\right) \tag{2}$$

where the respective ionic radii for the A, B, and oxygen ions are denoted by r_A, r_B, and r_O. With the assumption that the material is isotropic, the Williamson-Hall equation (WH-E) [27, 28] is a tool to compute the crystallite size ($D_{W\text{-}H}$) and the strain (ε) according to the following equation.

$$\beta\cos\theta = \frac{k\lambda}{D} + 4\varepsilon\sin\theta \tag{3}$$

The intersection of the relationship between $\beta\cos\theta$ and $4\sin\theta$ is used to calculate $D_{W\text{-}H}$, while the slope is used to calculate $\boldsymbol{\varepsilon}$, as depicted in Fig. 1(c). The calculated parameters are presented in Table 1. The total defects in the samples are characterized by the dislocation density (δ). The compositional dependence of $\boldsymbol{\varepsilon}$ and D is indicated by a shift in the XRD peaks relative to the parent phases.

There are multiple factors that affect the size of NCs that are worth noting. These factors include the relative ratio of the constituent phases, the grinding time, the sintering temperature, and the lattice mismatch between the planes of the CFO and SFO phases, among others. The tensile lattice strain is confirmed by positive values of ε, while the compressive property is indicated by a negative slope. The decrease in size of the NCs with increasing x ratios can be attributed to the increase in ε and δ resulting from physical interaction at the boundaries. This, in turn, leads to an increase in imperfections and deficiencies in the samples.

HRTEM analysis

Figure 2(a)–(e) depict the morphological properties, shape, size, and distribution of NPs from different NCs and parent samples

using HRTEM with the selected area electron diffraction pattern (SAED).

The SAED patterns exhibit clustered concentric rings with spots on the rings, confirming the XRD data and highlighting the excellent crystallinity of the NPs. The HRTEM micrographs of the analyzed samples reveal agglomerated NPs with roughly polygonal forms, suggesting physical interaction along the interfacial boundaries between the ferromagnetism and antiferromagnetism of the NPs [29]. The particle size of the NCs and the sample micrographs indicate that the NPs tend to aggregate and accumulate to maintain a lower free energy state due to dipole–dipole interaction [30].

FESEM, and EDAX analyses

Figure 3(a)–(e) illustrates FESEM images, and EDAX analyses for (1-x) CAFO + (x) SFO NCs (x = 1, 0.7, 0.5, and 0.3). The grains of the samples where x > 0 have irregular shape, random size distribution, agglomeration, inhomogeneity, and porosity, indicating the presence of the two phases from the parent samples. The decrease in grain size with increasing SFO is due to a higher rate of grain agglomeration. This suggests that SFO has a stronger binding ability, resulting in a more compact structure [31].

The EDAX report and spectrum provide the chemical analysis of the samples, revealing the presence of Sm, Co, Al, Fe, and O. The atomic (At %) and weight (wt%) percentages for each element are shown. The intensity of the peaks for each element confirms the stoichiometric ratio of the spinel-perovskite structure in each sample. The experimental and theoretical data on atomic and weight percentages are in good agreement.

In addition, Gwyddion 2.50 software is used to investigate the FESEM micrographs. This procedure is used to scrutinize the surface roughness of the studied NCs. Figure 4(a)–(d) displays the obtained micro graphs of the investigated NCs (x = 1, 0.7, 0.5, and 0.3). The images demonstrate that the samples have hillocks along the entire surface roughness. When more significant data is needed, sophisticated parameters can be clarified to further describe a surface.

The distribution of spikes above and below the mean plane is calculated using Rku. Rku is > than 3 for spiky surfaces and < than 3 for bumpy surfaces. All of the studied samples have bumpy surfaces, as indicated by the value of Rku.

As the SFO percentage increases, the surface becomes nearly spiky (x = 1). Ultimately, characterizing materials according to their degree of roughness can provide information about sample effectiveness across a wide range of application areas.

XPS analysis

Figure 5(a)–(c) illustrates the XPS analyses of the virgin materials for CAFO, SFO, and for x = 0.5 NCs, respectively.

TABLE 1: The average crystallite size by different methods, strain (ε), dislocation density (δ), and tolerance factor (T) for (1-x) CAFO + (x) SFO NCs.

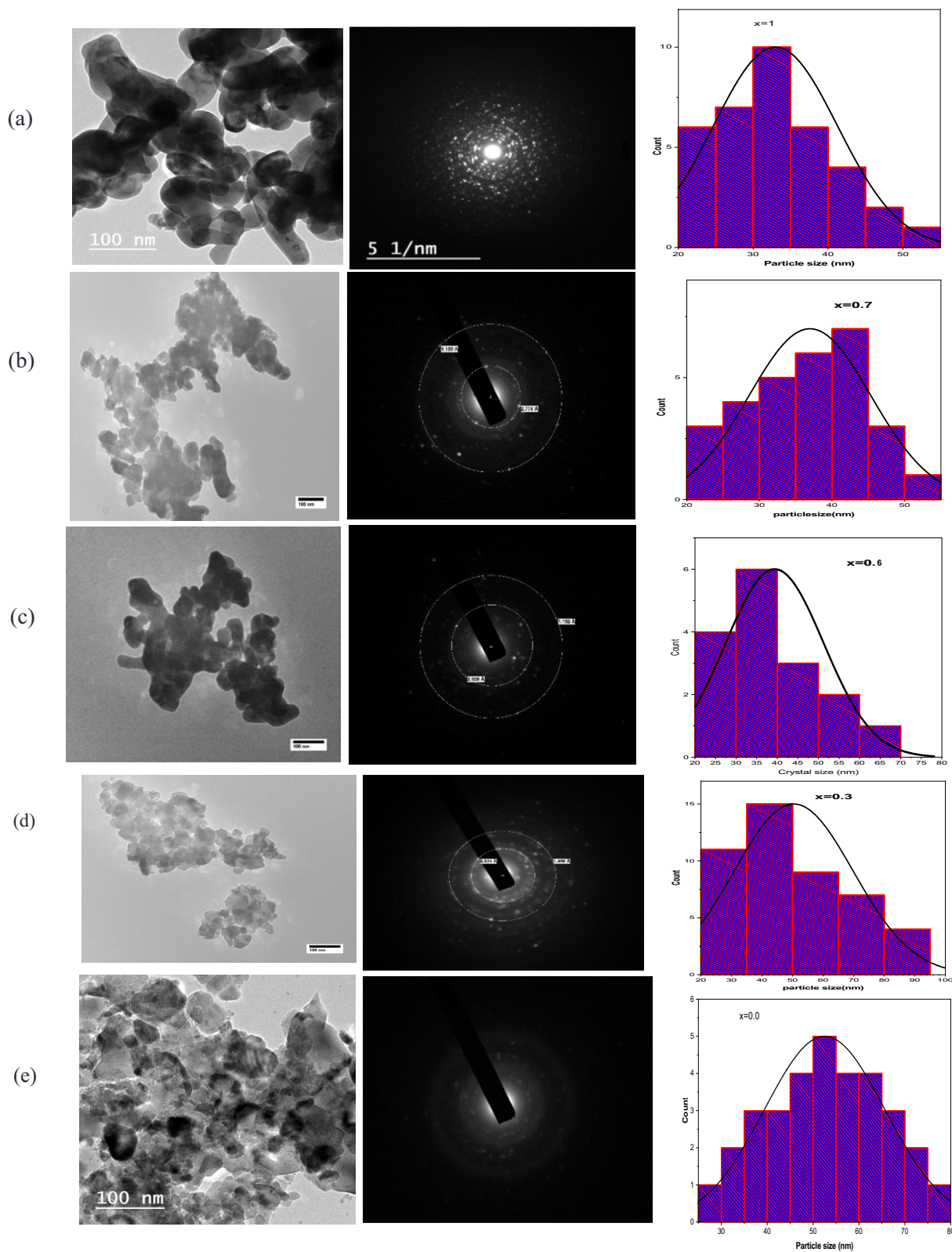| Sample (x)	(D) from W–H plot (nm)	(ε) 10⁻³	(δ) (lines/m²)10¹⁶	T
1(SFO)	35.461	− 0.755	7.952	0.810
0.7	36.488	2.330	7.511	–
0.5	37.373	2.120	71.595	–
0.3	38.730	1.800	6.667	–
0.0(CAFO)	40.901	0.312	5.978	1.011

Figure 2: (a)–(e) The micrographs, selected area electron diffraction (SAED), and particle size distribution histogram obtained from HERTEM analysis for (1-x) CAFO + (x) SFO nano-composites (where x= 1, 0.7, 0.5, 0.3, and 0.0).
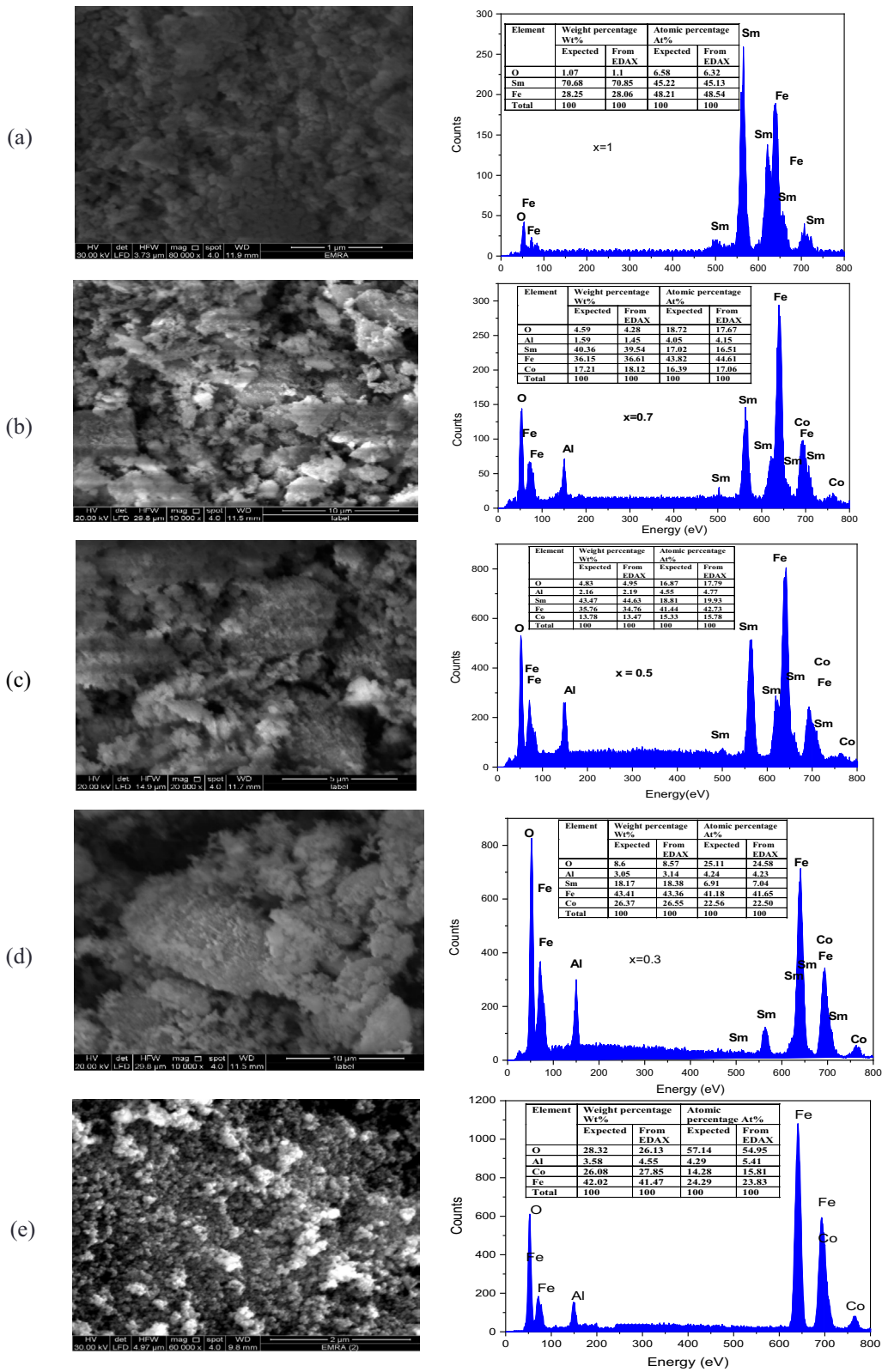
Figure 3: (a)–(e) The micrographs, and EDAX analysis for (1-x) CAFO + (x) SFO NCs (x= 1, 0.7, 0.3, and 0.0).
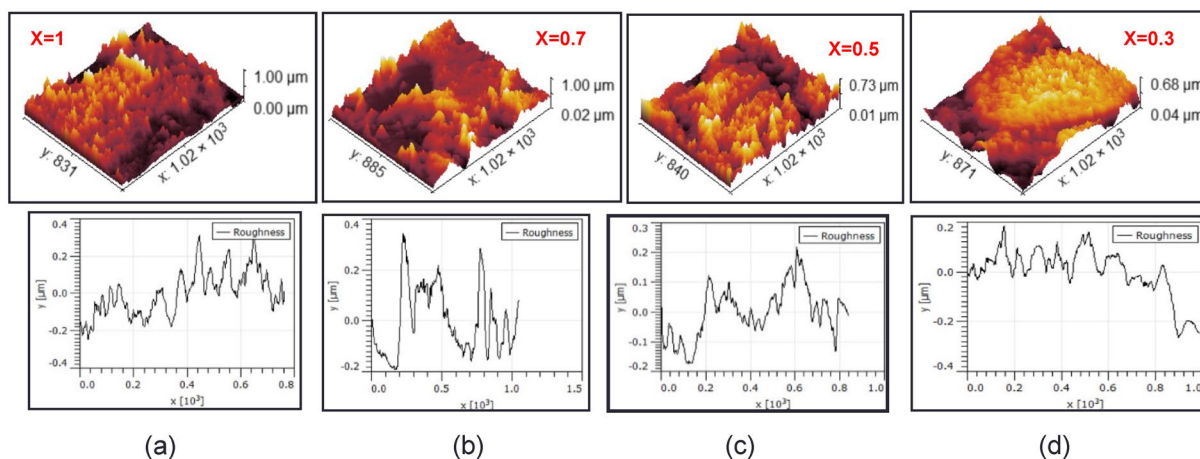
Figure 4: (a)–(d) The roughness images for (1-x) CAFO + (x) SFO nano-composites (x= 1, 0.7, 0.5, and 0.3).

The observed peaks are fitted to multiple peaks due to spin–orbit coupling and multiple splitting phenomena, [32]. The Co 2p spectrum consists of two spin–orbit doublets Co $2p_{1/2}$ and Co $2p_{3/2}$ that have different binding energies (B.E.) by 16.28 eV. Co $2p_{3/2}$ is split into 4 peaks at 780.74 eV, and 782.16 eV corresponding to Co^{2+} and Co^{3+} in B sites respectively, and SAT peaks at 785.33, 788.44 eV. Due to the spin–orbit coupling, the Fe 2p peaks can be fitted into Fe $2p_{1/2}$ and Fe $2p_{3/2}$. Fe $2p_{3/2}$ is fitted into 4 peaks and sat peaks at 711.17, 719.75, 713.58, and 716.52 with an atomic % of about 74.65%. The detected data indicate that the Fe^{3+} valence state is about 70% atomic % at the B sites and 30% at the A sites [33, 34]. The O1s spectra have numerous peaks at various B.E, with the strongest one at 531.56 eV relating to the oxide lattice and the others at 530.24 eV and 533.15 eV corresponding to the oxygen-deficient zone and connected to O^2, OH, air, water, and ad-sorption O/H_2O [34, 35]. The Al 2p peak detected at B.E $\cong$ 74.49 eV indicates the successful doping of Al^{3+} in the cobalt ferrite NPs.

The chemical properties of the surface and valence states of SFO NPs are scrutinized in Fig. 5(b). The XPS spectra show intense peaks for Sm, Fe, and O elements. The presence of Sm is ratified by the existence of two main peaks $3d_{3/2}$ and $3d_{5/2}$ which detect at B.E. of 1109.52 and 1081.98 eV, respectively [36].

The Fe 2p spectra are split into two spin–orbit doublets, corresponding to Fe $2p_{3/2}$ and Fe $2p_{1/2}$. The low energy Fe $2p_{3/2}$ peak (710.38 eV) is fitted with two peaks, both associated with Fe^{3+} ions at the B and A sites [37].

The O1s spectrum exhibits a pair of peaks at B.E. of 529.18 eV and 531.38 eV. The smaller B.E. of 529.18 eV matches O-F bonds and the higher B.E. peak represents a combination of O bonds with Sm and C, where the O–C is related to carbon tape.

Magnetic measurements

Hysteresis loops

Hysteresis loops and the fitted Langevin plot were used to analyze the magnetic properties of the (1-x) CAFO + (x) SFO NCs at $x = 0.5$, as shown in Fig. 6(a)–(b) The decrease in magnetization of the NCs with increasing Sm concentration can be attributed to the low magnetic nature of SFO samples. The saturation magnetization (Ms) at $x = 0.5$ was determined to be 27.35 emu/g at 20kOe using VSM measurements. Alternatively, the Ms value can be approximated by extrapolating the plot of magnetization versus $1/H^2$ to approach zero, based on the Stoner-Wohlfarth theory [38]. Using this method, the Ms value was found to be 27.4 emu/g.

The hysteresis loop of SFO ($x = 1$) at 300 K is shown in the inset of Fig. 6(a). It is characterized by a lack of saturation, a large width, and extremely low saturation (Ms) and remnant (Mr) values. This behavior can be explained by the partial alignment of the canted Fe^{3+} spins, where the magnetic properties are solely influenced by Fe^{3+}-Fe^{3+} interactions. Additionally, there are no Sm^{3+}-Sm^{3+} and Fe^{3+}-Sm^{3+} interactions present at low temperatures (5 K and 135 K) [39].

The smaller particle size of the virgin sample ($SmFeO_3$) is the main reason for the increase in coercivity (Hc) at ambient temperature [40]. According to the Dzyaloshinsky-Moriya theory, the Fe^{3+} ion spins in the virgin sample are not perfectly antiparallel to those of their surroundings, resulting in antiferromagnetic (AFM) behavior [41].

In contrast, the CAFO sample exhibits ferromagnetic (FM) behavior, as depicted in the figure, with a high value of Ms (53.79 emu/g).

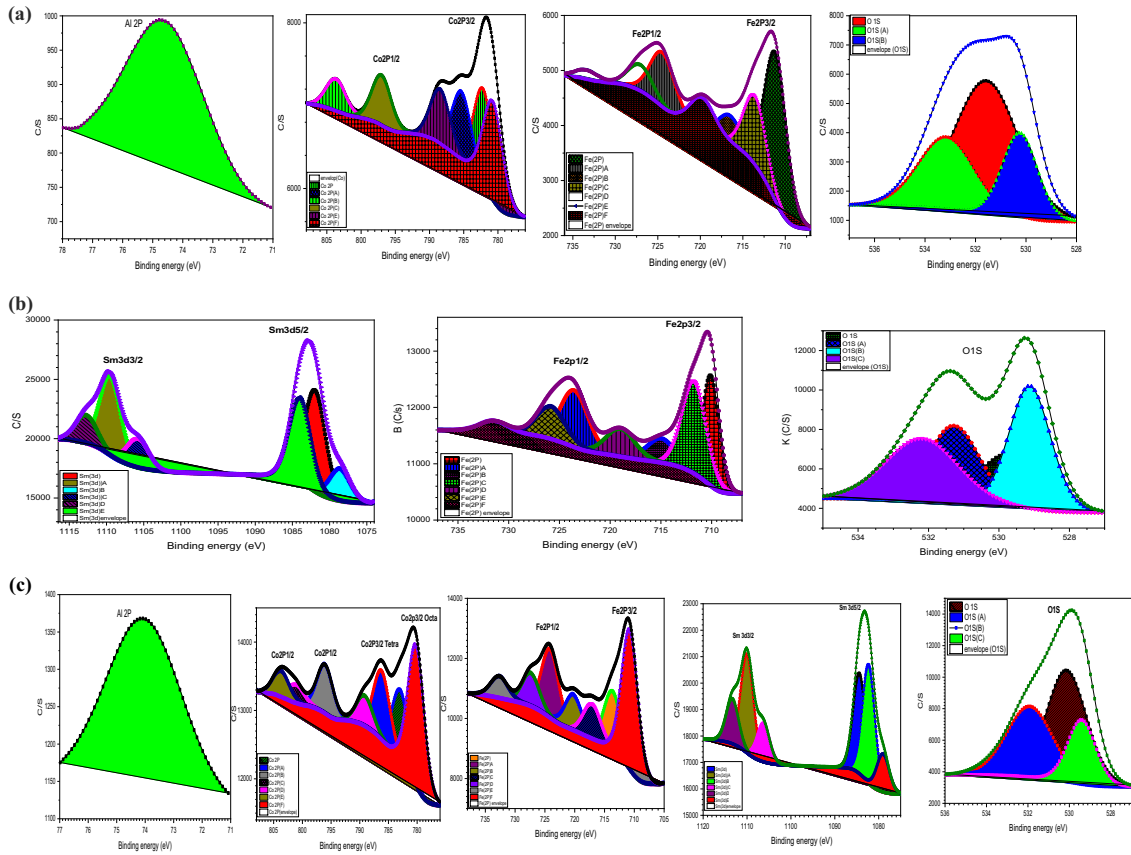Therefore, the type of magnetic ordering is the most significant factor in the observed magnetic behavior of the

Figure 5: (a)–(c) XPS analysis for Al, Co, Fe, O, Sm elements, of (1-x) CAFO + (x) SFO (x= 1, 0,0, and 0.5) NCs

nanocrystals (NCs). It is important to note that the addition of Al to Co ferrite decreases the magnetization of the system.

The observed magnetic parameters including Hc, Mr, Ms, R, magnetic anisotropy (K), and exchange bias field (H$_{EB}$), are listed in Table 2. The existence of magneto-static interactions [42] can be confirmed from the values of the R ($0 \leq R \leq 1$). Inter-granular magneto static interactions exist along the borders of the interfacial grains, as shown by non-zero values of the R for (1-x) CAFO + (x) SFO NCs.

Additionally, Eq. (4) can be used to quantify the amount of inter-granular magneto-static interactions in the produced NCs based on the approximated law of Vegard [43]

$$M_{Cal} = (1 - x)M_{CAFO} + (x)M_{SFO} \qquad (4)$$

The measured Mr of the spinel and perovskite parent phases is M$_{CAFO}$ and M$_{SFO}$ respectively, while M$_{cal}$ is the calculated Mr of the NCs. The measured and calculated values are presented in the Table. Except at ($x = 0.7$), it is detected that the measured values of Mr for NCs are lower than the calculated ones. This is attributed to the spin alignment at

the interfacial grain boundaries, exchange energy, and strain energy of the NCs being altered as a result of the magnetic coupling between the two phases. [44].

A small change in the hysteresis loop is observed in Fig. (6), which is caused by the ratio between the FM and AFM phases. This indicates that when two magnetic materials with different spin structures are in close proximity, the interface effects are important. The H$_{EB}$ values are calculated based on the horizontal displacement at the midpoint of the hysteresis loop for the specific concentration [45, 46].

$$H_{EB} = \frac{-\left(H_{left} + H_{right}\right)}{2} \qquad (5)$$

Table 2 presents the variation in H$_{EB}$ values at different concentrations (x). The H$_{EB}$ value exhibits a rapid increase from $x = 0.0$ to $x = 0.3$, followed by a subsequent decrease. This phenomenon can be attributed to the emergence of the EB effect in the synthesized nanometric systems. In these systems, the uncompensated surface spins favor antiferromagnetic (AFM) coupling, while the core of the particle favors ferromagnetic (FM) coupling.

As a result, natural AFM/FM interfacial boundary interfaces are formed, leading to the EB effect [47]. This suggests that the sample with $x = 0.3$ can be considered as a multilayer magnetic system with internal magnetic exchange interaction between interfacial boundary interfaces of AFM/FM. Finally, the H_{EB} is essential and is effective in various electronic applications, including ultrahigh-density magnetic recording and spin valve devices [48].

The value of the anisotropy constant K is calculated using the following equation [20] and the resulting data is summarized in the Table.

$$K = \frac{H_c x M_s}{0.98} \qquad (6)$$

The K value for the NCs increases significantly with an increase in spinel content. Specifically, at $x = 0.3$ and $x = 0.0$, the K values are nearly 11 and 17 times greater than at $x = 1$ (SFO). This indicates that the magnetization of the critical Nano-composite sample aligns in the hard direction, as opposed to SFO which aligns along the easy direction [43].

Microwave high frequency (MWHF) of NCs

Magnetic materials are in high demand for high-frequency systems like radar and telecommunications. Unlike metals, ferrites are non-conductive oxides that allow for the full penetration of electromagnetic fields [49]. However, at high frequencies, domain walls are unable to keep up with the fields, leading to spin dynamics absorbing microwave energy. The Landau-Lifshitz equation of motion [50] provides a classical explanation of this phenomenon, which can be expressed in its un-damped form [51] as follows:

$$\frac{dM}{dt} = \gamma M x H_i \qquad (7)$$

where M, γ, and H_i are magnetization, gyromagnetic ratio, and the whole interior field acting on the spin, respectively. The ratio between the mechanical and magnetic moment is characterized by γ which is given by Eq. (8) [52]

$$\gamma = \frac{ge}{2m_e} = \frac{g\mu_B}{\hbar} \qquad (8)$$

where μ_B is related to the Bohr magneton with its value in SI units as ($e\hbar/2m_e$), while (g) is the Landé splitting factor that controls the rate by which the energy levels split according to its magnitude, e^-, m_e, and $\hbar$ are charge, the mass of the electron, and the reduced Plank's constant respectively. The orbital g-factor for an e^- is estimated to be gL = 1 and the spin g-factor is calculated as gS $\cong$ 2. The Landé g-factor for the ground state is g = gS = 2 ($L = 0$, $J = 1/2$).

Recent research has revealed that the absorption of microwave frequency (MWF) by ferrites is affected by defects and the distribution of anisotropy field. This has highlighted the significant role of grain boundaries in the physical origin of losses in polycrystalline ferrites [53]. In some applications of ferrites, the interaction with the microwave field is controlled by exploiting the dependence of spin rotation on the orientation of the external field. When the field is aligned in one direction, the ferrite transmits the microwave field, while in the opposite direction, it strongly absorbs it. To determine if the investigated nanocrystals (NCs) are suitable for high-frequency wave (HFW) applications, the MWF value can be estimated using a specific equation [54].

$$\omega_m = 8\pi^2 M_s \gamma \qquad (9)$$

Table 2 presents a comprehensive list of the operating microwave frequencies (MWF) for nano-circuits (NCs). Based on the estimated data, it is evident that NCs can function within a frequency range of 0.1 to 11.9 GHz. All NCs produced exhibit a spectrum of frequencies that are suitable for the development of nanotechnology devices. These devices are designed to operate at higher frequencies, ranging from the S-band to the Ku band, enabling the transmission of radio waves. The operational MWF of the NCs, as determined through magnetic analysis, is depicted in Fig. 6-c. The frequency ranges at which the NCs can operate are influenced by various factors, such as the shape of the devices and the magnetic properties of the nanomaterials.

The switching field distribution field (SFD)

The SFD can be utilized to quantify the size of the hysteresis loop of the magnetic recording material in the second quadrant curve. It is also used to evaluate the extent of the hysteresis loop rectangle.

Figure 7 illustrates the SFD for the (1-x) CAFO + (x) SFO in relation to H. The value of SFD is determined using the equation [20, 46] below.

$$SFD = \frac{\Delta H}{H_c} \qquad (10)$$

By differentiating the hysteresis loops, $\frac{dM}{dH}$ is achieved, in which ΔH is the width at ½ the maximum peak of the $\frac{dM}{dH}$ curve. The smaller the SFD, the smaller the ½ width of the $\frac{dM}{dH}$ peak and the better the M_r/M_s.

The $\frac{dM}{dH}$ curve exhibits two distinct peaks, which is a common feature of a two-step reversal process. This double peak pattern is indicative of the interplay between exchange coupling and strong dipolar interactions. When the energies of exchange coupling and dipolar field are comparable, a double peak derivative is observed, with the first peak typically occurring prior to reaching zero fields from the saturation field [46].

The size frequency distribution (SFD) is affected by a key parameter known as HC, which peaks at $x = 1$ and decreases as x (SFO content) decreases. Conversely, the SFD exhibits a low value at $x = 1$ and increases as x increases, as shown in Table 2.

Therefore, it can be deduced that the x content influences the SFD values, which could result in change in particle size distribution. This variability may be due to the occupation of A and B sites, ultimately affecting the structure, size, and size disparity.

In conclusion, it is recommended to use composites with a low surface-to-volume ratio (SFD) for storage and recording purposes, whereas composites with a higher SFD are better suited for applications that necessitate targeted drug delivery and other faster responses [55].

The structural and magnetic parameters obtained for (1-x) $CoAl_{0.3}Fe_{1.7}O_4$ /(x) $SmFeO_3$ NCs are notably higher than those of previously studied samples, as demonstrated in Table 3.
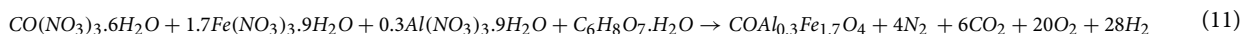
Conclusion

The coupling of $CoAl_{0.3}Fe_{1.7}O_4$ spinel and $SmFeO_3$ perovskite materials lead to new and enhanced structural and magnetic properties that neither component could achieve on its own

The CAFO/SFO nano-composites and their parent samples are produced using a modified citrate auto-combustion technique, to ensure the absence of any secondary phases. XRD,

waves traveling through the S-band to the Ku band. Operating frequency ranges are influenced by a variety of parameters, including the shape of the devices and the magnetism of the nanomaterial.

Experimental

SFO and CAFO NPs were synthesized using the citrate-gel auto-combustion method with citric acid serving as a fuel to enhance system homogeneity. Samarium nitrate (Sm $(NO_3)_3.6H_2O$), ferric nitrate (Fe$(NO_3)_3 \cdot 9H_2O$), cobalt nitrate(Co$(NO_3)_2.6H_2O$), aluminum nitrate (Co$(NO_3)_3.6H_2O$) and citric acid ($C_6H_8O_7 \cdot H_2O$) were used as starting materials. The raw materials were weighed according to stoichiometric ratio and dissolved in a minimal amount of distilled water. Citric acid was added in a 1:1 molar ratio to the metal nitrates. The pH of the solution was adjusted to 7 by dropwise addition of ammonia with constant magnetic stirring. The solution was heated on a hot plate until excess free water evaporated, followed by ignition. The combustion reaction was completed within in a few seconds. The collected powder was grinded for 2 h using a gate mortar and then heated at 600 °C for 1 h at a rate of 4 °C/min followed by grinding the powder for an additional 2 h. SFO powder was thoroughly mixed with CFO and grinded for 2 h at room temperature with different ratios (30:70, 50:50 and 70:30). The nanocomposite samples were sintered at 200 °C for 2 h at rate of 4 °C/min according to the following equations.

$$CO(NO_3)_3.6H_2O + 1.7Fe(NO_3)_3.9H_2O + 0.3Al(NO_3)_3.9H_2O + C_6H_8O_7.H_2O \rightarrow COAl_{0.3}Fe_{1.7}O_4 + 4N_2 + 6CO_2 + 20O_2 + 28H_2 \quad (11)$$

$$Sm(NO_3)_3.6H_2O + Fe(NO_3)_3.9H_2O + +C_6H_8O_7.H_2O \rightarrow SmFeO_3 + 3N_2 + 6CO_2 + 13O_2 + 20H_2 \quad (12)$$

FESEM, and XPS analyses confirm that the samples are physically created without any chemical interaction between the elements. The crystallite and particle sizes decrease with increasing SFO ratio. At the obtained nanoscale, the composite exhibits a higher surface area-to-volume ratio which can significantly recommend using them in waste water treatment as more active sites become available.

The weight ratios of the two phases (CAFO & SFO) in the NCs significantly affect H_{EB}. As x increases, the SFD will change from a low value at $x = 1$ ($SmFeO_3$) to a higher value, indicating that SFD can be adjusted by varying the SFO content. SFD have their maximum values for $x = 0.0$ and their minimum value for $x = 1.0$ resulting in a variety of applications such as in storage and recording field for low values and targeted drug delivery and other faster applications for high values. The NCs can operate at a frequency between 0.1 and 11.9 GHz making them suitable for the creation of nanotechnology devices from radio

X-ray powder diffraction (XRD) was used in the investigation of the crystallinity of the samples with a Bruker advanced D8 X-ray diffractometer. The pattern was recorded using Cu–Ka radiation ($\lambda = 1.54182$ A˚) in the 2θ range 20–80º, with a step size of 0.0130 and a scan step time of 3.5700 s.

The samples' morphology, mean particle size, grain size, and chemical composition were examined using a high-resolution transmission electron microscope (HRTEM) type JEOL-JEM 2100 and a high field emission scanning electron microscope (HFESEM, type Philips-UANTA FEG 250) linked with an EDAX unit (Energy Dispersive X-ray Analysis). X-ray photoelectron spectra (K-ALPHA; Thermo Fisher Scientific USA) of monochromatic X-ray Al K-alpha radiation were used to analyze the valence states and distribution of the elements in the samples. The room-temperature magnetic hysteresis of the nanocomposites was measured at a maximum field of 20 kOe using a vibrating sample magnetometer (VSM) model (Lake Shore 7410, USA).
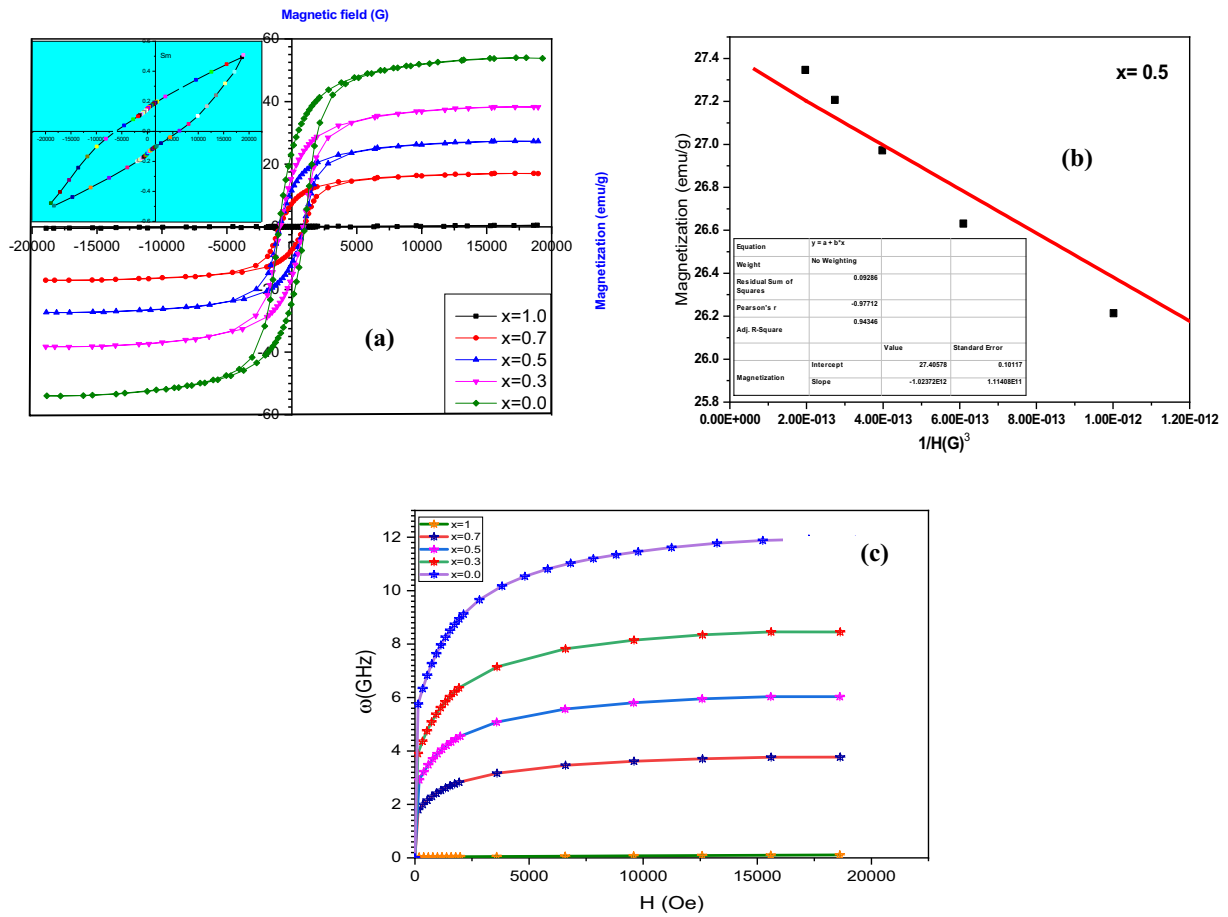
Figure 6: (a) The M-H hysteresis loops for (1-x) CAFO + (x) SFO NCs (x = 1, 0.7, 0.5, 0.3, and 0.0), (b) fitting plot between M versus $1/H^2$ (x=0.5). (c) Operating frequency as a function of applied magnetic field.

TABLE 2: The Ms, Mr, Hc, R, K, the calculated remnant magnetization (Mr(Cal), Exchange bias (H_{EB}), switching field distribution (SFD), and the operating frequency of micro wave for (1-x) CAFO + (x)SFO nano-composites (x = 1, 0.7, 0.5, 0.3, and 0.0).

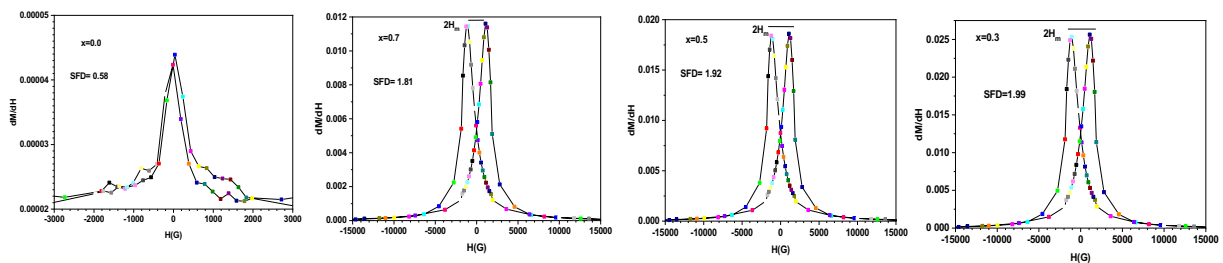| Conc.(x)	Ms (emu/g)	Mr (emu/g)	Hc (G)	Mr/Ms	K(10^4) (emu.G/g)	Mr (cal) (emu/g)	H_{EB}	SFD	ω_m (GHz)
1.0 (SFO)	0.51	0.149	6181	0.293	0.32	–	0.20	0.73	0.112
0.7	17.078	7.430	927	0.435	1.62	7.27	4.14	1.81	3.78
0.5	27.35	11.690	914	0.427	2.55	12.00	3.14	1.92	6.05
0.3	38.32	16.052	891	0.419	3.48	16.75	1.98	1.99	8.5
0.0 (CAFO)	53.79	23.870	985	0.444	5.41	–	1.22	2.03	11.9

Figure 7: (a)–(d) Switching field distribution for (x) CAFO + (1-x) SFO NCs (x=0.0, 0.3, 0.5, and 0.7) at room temperature.

TABLE 3: Comparison of the present data and the data reported in the literature.

NCs	Size (nm)	Mr (emu/g)	Hc(G)	Ms (emu/g)	References
$(0.6)LaFeO_3 + (0.4)CoFe_2O_4$	–	12.1	2018	25.1	[22]
$(0.3)CoFe_2O_4 + (0.7)Sm_{0.7}La_{0.3}FeO_3$	–	11.2	1394	27.54	[21]
$(0.3) NFe_2O_4 + (0.7)BiFeO_3$	6.54	1.29	123.5	14.47	[31]
$(0.3) MnFe_2O_4 + (0.7)Bi_3FeO_3$	102	0.53	85.7	4.54	[56]
$(0.4)Cu_{0.3}Mn_{0.7}Fe_2O_4 + (0.6)La_{0.9}Bi_{0.1}FeO_3$	–	1.83	125	8.41	[29]
$(0.5) CoFe_2O_4 + (0.5) Bi_{0.8}La_{0.2}Fe_{0.12}Cr_{0.88}O_3$	30	23.9	1485	47.9	[57]
$(1-x)CoFe_2O_4/(x)SmFeO_3$ (x = 0.0, 0.3, 0,5, 0.7, and 1)	35.5–41	0.15–23.9	6181–891	0.5–53.8	Present study

Author contributions

KKM contributed to material preparation, data collection and analysis, formal analysis, investigation, optimum selection of material parameters, methodology, validation and visualization, review and editing. EEA contributed to conceptualization, validation, data curation, and analysis, formal analysis, writing–original draft preparation, writing–review & editing, visualization, and supervision. DNG contributed to material preparation, data curation, and analysis, formal analysis, investigation, optimum selection of material parameters, methodology, review and editing. FZG: Data curation; Formal analysis. CS: Validation, and, Visualization. AE-B: she was added according to university rules without any scientific contribution.

Funding

Data availability

The data supporting the findings of this study are available from the corresponding author upon reasonable request.

Declarations

Competing interests The authors declare no competing interests.

Open Access

References

1. S. Yu-Quan, Z. Wei-Ping, F. Yong, Y. Yan-Ting, W. Liao-Yu, W. Dun-Hui, D. You-Wei, Multiferroic properties in terbium orthoferrite. Chin. Phys. B **23**(7), 77505 (2014)

2. E. E. Ateia, D. Gawad, Mohamed Mosry, M. M. Arman, Synthesis and Functional Properties of La2FeCrO$_6$ Based Nanostructures, Journal of Inorganic and Organometallic Polymers and Materials, Published online 22 May (2023)

3. M.A. Farrukh, Advanced Aspects of Spectroscopy, InTech., Janeza Trdine 9, 51000 Rijeka, Croatia, pp. 373 First published August, (2012).

4. E.E. Ateia, Y. A. Saeid, Characterization of Core–Shell CaFe$_{1.925}$Sm$_{0.05}$Gd$_{0.025}$O$_4$ @ Polymer from Synthesis to Applications, Journal of Inorganic and Organometallic Polymers and Materials, Published online 29-July (2023).

5. E. E. Ateia, Y. A. Saeid, M. K. Abdelmaksoud, Synthesis and Characterization of CaFe$_{1.925}$Gd$_{0.025}$Sm$_{0.05}$O$_4$/PEG Core–Shell Nanoparticles for Diverse Applications, Journal of Superconductivity and Novel Magnetism, Published online 19 March (2023).

6. E.E. Ateia, A.T. Mohamed, Core-shell nanoarchitectonics of CoFe2O4 encapsulated La2Fe2O6 Nanoparticles for their use in various applications. J. Inorg. Organomet. Polym. Mater. **32**, 1389–1399 (2022)

7. A. Ehresmann, D. Lengemann, T. Weis, A. Albrecht, J. Langfahl-Klabes, F. Göllner, D. Engel, Adv. Mater. **23**, 5568–5573 (2011)

8. E.E. Ateia, B. Hussein, C. Singh, M.M. Arman, Multiferroic properties of GdFe0.9M0.1O3 (M= Ag1+, Co2+ and Cr3+) nanoparticles and evaluation of their antibacterial activity. Eur. Phys. J. Plus **137**, 443 (2022)

9. X. Fu, X. Zeng, D. Wang, H.C. Zhang, J. Han, T.J. Cui, Phys. Rev. B **87**, 184405 (2013)

10. H.T. Giang, H.T. Duy, P. Quang Ngan, G. Hong Thai, D.T. Anh Thu, D.T. Thu, N.N. Toan, Sens. Actuators B **158**, 246 (2011)

11. Y.K. Jeong, J.H. Lee, S.J. Ahn, H.M. Jang, Solid State Commun. **152**(13), 1112 (2012)

12. S. Cao, H. Zhao, B. Kang, J. Zhang, W. Ren, Sci. Rep. **4**, 5960 (2014)

13. B.V. Prasad, G. Narasinga Rao, J.W. Chen, D. Suresh Babu, Mat. Res. Bull. **46**, 1670–1673 (2011)

14. B. Purnama, A. Khoiriah, Suhatyana, Structural and magnetic properties of aluminum- substituted cobalt ferrite nanoparticles synthesized by the Co-precipitation Route. J. Magn. **23**(1), 106–111 (2018)

15. E.E. Ateia, O. Rabie, Amira T. Mohamed, Multi-susceptible single-phased hexaferrite with significant magnetic switching properties by selectively doping. Phys. Scr. **98**, 065801 (2023)

16. E.E. Ateia, A. Al-Hamzi, B. Hussein, Synthesis and characterization of nonstoichiometric cobalt nanoferrites for multifunctional applications. J. Mater. Sci.: Mater. Electron. **33**, 20642–20655 (2022)

17. E.E. Ateia, R. Ramadan, A.S. Shafaay, Appl. Phys. A **126**, 222 (2020)

18. S.M.Hosseimpour—Mashkani, M.Maddahfar, A.Sobhani-Nassab. Precipitation,synthesis, characterization, Moorphological, control and photo catalyst application of mater.45, 3612(2016)

19. B.K. Kuanar, S.R. Mishra, L. Wang, D. Delconte, D. Neupane, V. Veerakumar, Z. Celinski, Mat. Res. Bull. **76**, 22 (2016)

20. E.E. Ateia, K.K. Meleka, F.Z. Ghobrial, Interplay between cation distribution and magnetic properties for $CoAl_xFe_{2-x}O_4$ ($00 \leq x \leq 0.7$) nanoparticles. Appl. Phys. A **127**, 831 (2021)

21. E.E. Ateia, M.K. Abdemaksoud, H. Ismail, A study of the magnetic properties and the magnto-crystalline anisotropy for the nano-composites $CoFe_2O_4/Sm_{0.7}La_{0.3}FeO3$. J. Mater. Sci.: Mater. Electron. **32**, 4480–4492 (2021)

22. E.E. Ateia, M.K. Abdemaksoud, M.A. Rizk, Improvement of the physical properties of novel $(1–x)$ CoFe2O4 (x) LaFeO3 nanocomposite for technological applications. J. Mater. Sci.: Mater. Electron. (2017). https://doi.org/10.1007/s10854-017-7567-1

23. J. Lian, K.B. Helean, B.J. Kennedy, L.M. Wang, A. Navrotsky, R.C. Ewing, J. Phys. Chem. B **110**, 2343 (2006)

24. V.M. Goldschmidt, Naturwissenschaften **14**, 477 (1926)

25. R.J. Hill, J.R. Craig, G.V. Gibbs, Phys. Chem. Miner. **4**, 317 (1979)

26. M.A. Ahmed, N.G. Imam, M.K. Abdelmaksoud, Y.A. Saeid, Magnetic transitions and butterfly-shaped hysteresis of Sm-Fe-Al-based perovskite-type orthoferrite. J. Rare Earths **33**(9), 965–971 (2015)

27. V.D. Mote, Y. Purushotham, B.N. Dole, Williamson-Hall analysis in estimation of lattice strain in nanometer-sized ZnO particles. J. Theor. Appl. Phys. **6**, 6 (2012)

28. S. Mustafa et al., Comparative study of crustallite size using Williamson-Hall and Debye-Scherrer plots for ZnO manoparticles. Adv. Nat. Sci.: Nanosci. Nanotechnol. **10**, 045013 (2019)

29. E.H. El-Khawas, The effect of the interface on magnetic properties of perovskite-spinel nanocomposites arab. J. Nucl. Sci. Appl. **52**(3), 232–241 (2019)

30. E.E. Ateia, H. Ismail, H. Elshimy, M.K. Abdelmaksoud, Structural and magnetic tuning of LaFeO3 Orthoferrite substituted diferent rare earth elements to optimize their technological applications. J. Inorg. Organomet. Polym Mater. **31**, 1713–1725 (2021)

31. P. Augustine, Y. Narayana, N. Kalarikkal, An effective strategy for development of multiferrioc composite nanostructures with enhanced magnetoelectric coupling performance a perovskitee-spinel approach. Nanoscale Adv. **3**, 4866 (2021)

32. S.U. Rather, H. Bamufleh, H. Alhumad, Structural, thermal, morphology, surface, chemical and magnetic analysis of Al^{3+} doped nano structured mixed-spinel cobalt ferrites. J. Ceram. Int **47**, 17361 (2021)

33. S.R. Naik, A.V. Salker, Change in the magneto structural properties of rare earth doped cobalt ferrites relative to the magnetic anisotropy. J. Mater. Chem. **22**, 2740–2750 (2012)

34. R.S. Yadav, I. Kuˇritka, J. Vilcakova, J. Havlica, J. Masilko, L. Kalina, J. Tkacz, J. Svec, V. Enev, M. Hajdúchova, Impact of grain size and structural changes on magnetic, dielectric, electrical, impedance and modulus spectroscopic characteristics of $CoFe_2O_4$ nanoparticles synthesized by honey mediated sol-gel combustion method. Adv. Nat. Sci. Nanosci. Nanotechnol. **8**, 045002 (2017)

35. Vinuthna, D. Ravinder, R.M. Raju, Characterization of $Co_{1-x}Zn_xFe_2O_4$ Nano spinel ferrites prepared by citrate precursor method. Int. J. Eng. Res. Appl. **3**(6), 654–600 (2013)

36. W. Fan, Z. Sun, J. Wang, J. Zhou, K. Wu, Y. Cheng, A new family of Ce-doped $SmFeO_3$ perovskite for application in symmetrical solid oxide fuel cells. J. Power. Sources **312**, 223–233 (2016)

37. Y. Zhang, H. Zou, J. Peng, Z. Duan, M. Ma, X. Xin et al., Enhanced humidity sensing properties of $SmFeO_3$-modified MoS_2 nanocomposites based on the synergistic effect. Sens. Actuat B Chem. **272**, 459–467 (2018)

38. A. Sasmal, S. Sen, P.S. Devi, Synthesis and characterization of $SmFeO_3$ and its effect on the electrical and energy storage properties of PVDF. Mater. Res. Bull. **130**, 110941 (2020)

39. A. Ahlawat, S. Kushwaha, A.A. Khan, S. Satapathy, Influennce of particle size on spin switching properties and magneto electric coupling in SmFeO3. J. Mater. Sci. Mater. Electron. **29**, 927–934 (2018)

40. Q. Hu, B. Yue, D. Yang, Z. Zhang, Y. Wang, J. Liu, Electrochemical and magnetic properties of electrospun $SmFeO_3$ and $SmCoO_3$ nanofibers. J. Am. Ceram. Soc. **105**, 1149–1158 (2022)

41. Berthomieu, E. Nabedryk, W. Mantele, J. Breton, Characterization by FTIR spectroscopy of the photoreduction of the primary

quinone acceptor QA in photosystem II. FEBS Lett. **269**(2), 363–367 (1990)

42. O.G. Udalov, N.M. Chtchelkatchev, I.S. Beloborodov, Coupling of ferroelectricity and ferromagnetism through Coulomb blockade in composite multiferroics. Phys. Rev. B **89**, 174203 (2014)

43. A.M. Belemuk, O.G. Udalov, N.M. Chtchelkatchev, I.S. Beloborodov, Competition of magneto-dipole, anisotropy and exchange interactionsin composite multiferroics. J. Phys.: Condens. Matter **28**, 126001 (2016). https://doi.org/10.1088/0953-8984/28/12/126001

44. C. Frandsen, C.W. Ostenfeld, M. Xu, C.S. Jacobsen, L. Keller, K. Lefmann, S. Mørup, Interparticle interactions in composites of nanoparticles of ferromagnetic (γ-Fe_2O_3) and antiferromagnetic (CoO, NiO) materials. Phys. Rev. B **70**, 134416 (2004)

45. E.E. Ateia, M.A. Ateia, M.M. Arman, Assessing of channel structure and magnetic properties on heavy metal ions removal from water. J. Mater. Sci. Mater. Electron. **33**, 8958–8969 (2022). https://doi.org/10.1007/s10854-021-07008-9

46. Y.Y. Wang, C. Song, F. Zeng, F. Pan, Field- direction sensitive magnetization reversal in a perpendicularly exchange-coupled system. J. Phys. D Appl. Phys. **46**, 445001 (2013)

47. B.M. Tanygin, On the free energy of the flexomagnetoelectric interactions. J. Magn. Magn. Mater. **323**, 1899–1902 (2011)

48. S. Tanushree, S. Elizabeth, P.S. Anil Kumar, Electron doping induced exchange bias and cluster glass magnetism in multiferroic Sc0.8Zr0.2MnO3. J. Magn. Magn. Mater. **466**, 225 (2018)

49. M. Pardavi-Horvath, Microwave applications of soft ferrites. J. Magn. Magn. Mater. **215**, 171–183 (2000)

50. L.D. Landau, E. Lifshitz, On the theory of the dispersion of magnetic permeability in ferromagnetic bodies. Physik Z. Sowjetunion **8**, 153–169 (1935)

51. Raul Valenzuel, Novel applications of ferrites Hindawi publishing corporation. Phys. Res. Int. **2012**, 1–9 (2012)

52. Y. Alivov, H. Morkoç, Microwave ferrites, part 1: fundamental properties. J. Mater. Sci.: Mater. Electron. **20**(9), 789–834 (2009). https://doi.org/10.1007/s10854-009-9923-2

53. N. Mo, Y. Y. Song, and C. E. Patton, "High-field microwave effective linewidth in polycrystalline ferrites: physical origins and intrinsic limits," Journal of Applied Physics, 97, no. 9, Article ID 093901, pp. 1–9, (2005)

54. M.N. Akhtar, M. Saleem, M.A. Khan, J. Phys. Chem. Solids **123**, 260–265 (2018)

55. S. Kumar, R.R. Singh, P.B. Barman, Reitveld refinement and derivative spectroscopy of nanoparticles of soft ferrites (MgNiFe). J. Inorg. Organomet. Polym. Mater. **31**, 528–541 (2021)

56. K.P. Remya, R. Rajalakshmi, N. Panpandian, Development of BiFeO3/$MnFe_2O_4$ Ferrite nano composites with enhanced magnetic and electrical properties. Nanoscale Adv. **2**, 2968–2976 (2020)

57. S.F. Mansour, N.G. Imam, S. Goda, M.A. Abdo, Constructive coupling between BiFeO3 and $CoFe_2O_4$, promising magnetic and dielectric properties. J. Mater. Res. Technol. **2**, 1434–1446 (2020)

www.mrs.org/jmr

April 2024

Issue 7

Volume 39

Journal of Materials Research

1180